
The soft X-ray background with Suzaku II: Supervirial temperature bubbles?

Hayato SUGIYAMA¹, Masaki UEDA¹, Kotaro FUKUSHIMA¹, Shogo B. KOBAYASHI¹, Noriko Y. YAMASAKI², Kosuke SATO³ and Kyoko MATSUSHITA¹

¹Department of Physics, Tokyo University of Science, 1-3 Kagurazaka, Shinjuku-ku, Tokyo 162-8601, Japan

²Institute of Space and Astronautical Science, Japan Aerospace Exploration Agency, 3-1-1 Yoshinodai, Chuo-ku, Sagami-hara, Kanagawa 252-5210, Japan

³Graduate School of Science and Engineering, Saitama University, 255 Shimo-Okubo, Sakura-ku, Saitama, Saitama 338-8570, Japan

*E-mail: matusita@rs.tus.ac.jp

Received ; Accepted

Abstract

Observations of the hot X-ray emitting interstellar medium in the Milky Way are important for studying the stellar feedback and understanding the formation and evolution of galaxies. We present measurements of the soft X-ray background emission for 130 Suzaku observations at $75^\circ < l < 285^\circ$ and $|b| > 15^\circ$. With the standard soft X-ray background model consisting of the local hot bubble and the Milky Way halo, residual structures remain at 0.7–1 keV in the spectra of some regions. Adding a collisional-ionization-equilibrium component with a temperature of ~ 0.8 keV, much higher than the virial temperature of the Milky Way, significantly reduces the derived C-statistic for 56 out of 130 observations. The emission measure of the 0.8 keV component varies by more than an order of magnitude: Assuming the solar abundance, the median value is $3 \times 10^{-4} \text{ cm}^{-6} \text{ pc}$ and the 16th–84th percentile range is $(1\text{--}8) \times 10^{-4} \text{ cm}^{-6} \text{ pc}$. Regions toward the Orion-Eridanus Superbubble, a large cavity extending from the Ori OB1 association, have the highest emission measures of the 0.8 keV component. While the scatter is large, the emission measures tend to be higher toward the lower Galactic latitude. We discuss possible biases caused by the solar wind charge exchange, stars, and background groups. The 0.8 keV component is probably heated by supernovae in the Milky Way disk, possibly related to galactic fountains.

Key words: Galaxy:halo — X-rays:ISM — X-rays:diffuse background — ISM:structure

1 Introduction

Understanding star formation and stellar feedback is essential for studying the formation and evolution of galaxies. Supernovae (SNe) heat the interstellar medium (ISM). In star-forming regions, stellar wind or multiple SNe can create superbubbles filled with hot plasma (e.g. Hill et al.

2012; Keller et al. 2014; Kavanagh 2020). SNe may drive hot gas from the disk, create outflows or galactic fountains, and eject energy and metals into the intergalactic space (Dekel & Silk 1986; Tumlinson et al. 2017). In addition, accreting gas from the intergalactic space is expected to be heated to the virial temperature by shock waves generated by mass accretion (e.g., Rees & Ostriker 1977). We

can study these activities with X-ray observations of hot ISM in galaxies.

Suzaku, Japan's X-ray astronomy satellite, is characterized by its low background, allowing us to make a detailed study of the low-surface brightness X-ray emission from hot gas in the Milky Way. Such hot gas contributes to the soft X-ray background detected below ~ 1 keV. A spectral component modeled with a collisional-ionization-equilibrium (CIE) component at a temperature of ~ 0.2 keV is thought to originate from an extended, diffuse plasma in our Galaxy, called the Milky Way Halo (MWH) (e.g., Yoshino et al. 2009, Henley & Shelton 2013, Nakashima et al. 2018). A cavity filled with a CIE component at a temperature of 0.1 keV, thought to be created by SNe surrounding the Sun, is called the local hot bubble (LHB). In addition, to explain the spectra of some regions, Yoshino et al. (2009) needed a much higher Ne abundance ($\text{Ne}/\text{O} \sim 3$ solar) or an additional higher temperature (0.5–0.9 keV) component.

Sekiya et al. (2014a), Nakashima et al. (2018), and Gupta et al. (2021) also reported the presence of the 0.6–1.0 keV component from some regions observed with Suzaku. Gupta et al. (2023) analyzed Suzaku data from 230 fields and found a bright, supervirial temperature component from the eROSITA bubble (Predehl et al. 2020) that includes the North Polar Spur/Loop I structure. Their analysis also revealed that the emission measure of this supervirial component exhibits a dependence on the galactic longitude, with a significant increase toward the bubble. Bluem et al. (2022) also detected two hot gas model components, with temperatures of ~ 0.17 keV and ~ 0.7 keV, which are widely distributed across the Milky Way with the HaloSat at $|b| > 30^\circ$ and studied the dependence on the angular distance from the Galactic center. With eROSITA observations covering 142 square degrees ($220^\circ < l < 235^\circ$, $20^\circ < b < 40^\circ$), Ponti et al. (2023) also found a similar spectral component with temperature of 0.4–0.7 keV.

Ueda et al. (2022), hereafter Paper-I, analyzed Suzaku data from 130 observations ($75^\circ < l < 285^\circ$, $|b| > 15^\circ$) and reported that adding a hot CIE component with a temperature of ~ 0.8 keV (hereafter the 0.8 keV component) to the standard background model reproduces the spectra of a significant fraction of the observations. In addition, they suggested that O VII He α emissions, possibly from heliospheric solar wind charge exchange (SWCX), sometimes lead to underestimation and overestimation of temperatures and emission measures, respectively, of the MWH component. From the observations before the end of 2009, or excluding the data around the solar maximum, the temperature (~ 0.2 keV) of the MWH component is quite uni-

form. At $|b| < 35^\circ$, its emission measure increases toward the lower Galactic latitude, indicating the presence of a disk-like morphology component. In addition, they suggested that plasma with the virial temperature (~ 0.2 keV) of the Milky Way may fill the halo in nearly hydrostatic equilibrium.

This paper presents the results of the 0.8 keV component derived from the same observations as in Paper-I. The paper is organized as follows. In Section 2, we describe the observations and data reduction. In Section 3, we present spectral fitting results, the spatial distribution of emission measure of the 0.8 keV component, especially dependence on the Galactic latitude, and systematic uncertainties caused by the SWCX. In Section 4, we discuss the results. This paper uses the solar abundance table from Lodders (2003). Errors are reported at the 68% confidence level unless otherwise noted.

2 Observations and data reduction

We have analyzed the X-ray Imaging Spectrometer (XIS) data of the 130 observations at $75^\circ < l < 285^\circ$ and $|b| > 15^\circ$ with *Suzaku* presented in Paper-I. This excludes regions toward the Galactic center, the eROSITA bubble, and the Galactic disk. We also excluded the regions around very bright point sources and extended objects, such as galaxy clusters and supernova remnants. The XIS consists of four CCD sensors. XIS0, 2, and 3 contain front-illuminated (FI) CCDs and XIS1 has a back-illuminated (BI) CCD (Koyama et al. 2007). We analyzed four CCD data taken before the loss of XIS2 in November 2006. After the loss, we analyzed the data from the three remaining CCDs. Data obtained with 3×3 and 5×5 editing modes were merged. We applied the same filtering and point source removal as in Paper-I. To decrease the contamination caused by the SWCX, we created light curves and excluded the time ranges where the count rate exceeded 3σ . The details were described in Paper-I.

3 Spectral analysis and results

We extracted a spectrum over the field of view (FOV) of each XIS detector from each observation. We used the `xisrmfgen` tools task to create the redistribution matrix files (RMFs). To create ancillary response files, we used the `xissimarfgen` task assuming uniform emission from a circular region with a radius of $20'$. The instrumental background, or non-X-ray background (NXB), was estimated from the Night-Earth database using the `xisnxbgen` task. We used XSPEC version 12.10.1f (Arnaud 1996) to model the NXB-subtracted spectra. We used the energy ranges of

0.4–7.0 keV for the BI spectra, and 0.5–7.0 keV for the FI spectra. We rebinned each spectrum to have at least one count per bin and employed the extended C-statistic (Cash 1979). We used APEC (Astrophysical Plasma Emission Code, Smith et al. 2001, Foster et al. 2012) with AtomDB version 3.0.9 to model a CIE plasma.

3.1 The standard soft X-ray background model

We first applied the standard background model, hereafter referred to as Model-s. This model has four components: The cosmic X-ray background (CXB), two CIE components (“apec” model in XSPEC) to model LHB and MWH, and the O I $K\alpha$ line for the scattered photons from the sunlit atmosphere of the Earth (Sekiya et al. 2014b). We used a power-law model with a photon index of 1.4 to model CXB. We fixed the temperature of the LHB at 0.1 keV and the abundances of LHB and MWH at 1 solar. The CXB and the MWH were subject to photoelectric absorption due to cold gas. We modeled this absorption using the “phabs” model in the XSPEC spectral fitting tool, with a fixed hydrogen column density at the Galactic value from Kalberla et al. (2005). A Gaussian with fixed central energy of 0.525 keV was used to model the O I line. The normalization of each component was allowed to vary. The spectra of the XIS detectors of each observation were fitted simultaneously with Model-s. These fits are the same as in Paper-I, where the results for the MWH component were presented. In most cases, the temperatures of the MWH component (hereafter kT_{halo}) are in the range of 0.15–0.3 keV. However, as reported by Yoshino et al. (2009), Sekiya et al. (2014a), and Nakashima et al. (2018), some observations show significantly higher MWH temperatures around 0.6–1 keV. As shown in figure 1, with Model-s, there are residual structures around 0.7–1 keV in the spectra of some observations.

3.2 With a supervirial temperature component

We then added another “apec” component modified by the Galactic absorption to Model-s and fitted the spectra with this model. The temperature and abundance of this additional component were fixed at 0.8 keV and 1 solar, respectively. We will refer to this model as Model-08. This paper presents the results of the 0.8 keV component with Model-08, while those of the others were presented in Paper-I. As shown in figure 1, Model-08 can reproduce the spectra well. Out of 130 observations, 56 of them got $\Delta C < -9$. Here, ΔC is the C-statistic for Model-08 subtracted from that for Model-s. For observations with exposures longer than 60 ks, 35 out of 57 observations have

Table 1. Medians and 16th-84th percentile ranges of $EM_{0.8}$ with

Model-08			
selection	N*	median $10^{-4}\text{cm}^{-6}\text{pc}$	16th-84th percentile $10^{-4}\text{cm}^{-6}\text{pc}$
all	130	3.8	0.9–7.7
$ b \leq 35^\circ$	47	4.9	2.1–9.5
$35^\circ < b \leq 50^\circ$	42	3.8	0.8–6.8
$ b > 50^\circ$	41	2.3	0.6–4.6

* Number of observations

$\Delta C < -9$. Thus, almost half of the observations prefer Model-08 to Model-s, although some with the longest exposures have $\Delta C \sim 0$. The emission measure ($= \int n_{\text{H}} n_e ds$, where s is the distance along the line of sight) of the 0.8 keV component (hereafter $EM_{0.8}$) spans an order of magnitude; the median value and the 16th-84th percentile range of the 130 observations (including data with $\Delta C \geq -9$) are $3.8 \times 10^{-4} \text{ cm}^{-6}\text{pc}$ and $(0.9\text{--}7.7) \times 10^{-4} \text{ cm}^{-6}\text{pc}$, respectively (table 1). As reported in Paper-I, the median of kT_{halo} becomes 0.19 keV.

We then allowed the temperature of the 0.8 keV component to vary in the range of 0.6–1.4 keV and re-fitted the spectra of the observations with $\Delta C < -9$. We will refer to this model as Model-08-kTfree. As shown in figure 2, the temperatures of the 0.8 keV component, or $kT_{0.8}$, are concentrated around 0.8–1 keV. There are several regions with temperatures around 1.3 keV. There is no significant correlation between $EM_{0.8}$ and $kT_{0.8}$. $kT_{0.8}$ does not depend on the Galactic latitude or longitude.

In our analysis, we adopt the column density of the absorption, N_{H} as the Galactic value of the HI gas. If the 0.8 keV component is distributed inside the cold gas or coexists with it, we may overestimate both N_{H} and $EM_{0.8}$. Therefore, we refitted the spectra with Model-08, allowing N_{H} of the 0.8 keV component to vary, with an upper limit at the Galactic value. For most of the observations, the obtained values of $EM_{0.8}$ are in agreement with those obtained from Model-08. In section 4.3, we estimate the scale height of the 0.8 keV component, which is likely larger than several tens of pc for the HI and H₂ disks. Consequently, the majority of the 0.8 keV component might be located outside the cold gas disks, validating the use of the “Galactic value” for the spectral modeling.

3.3 Spatial distribution of the 0.8 keV component

Figure 3 shows $EM_{0.8}$ on the 3/4 keV band image of the ROSAT all-sky survey. The brightest $EM_{0.8}$ regions are concentrated toward the Orion-Eridanus superbubble (Reynolds & Ogden 1979; Brown et al. 1995) around $(l, b) \sim (200^\circ, -40^\circ)$. This bubble is a large cavity extending from

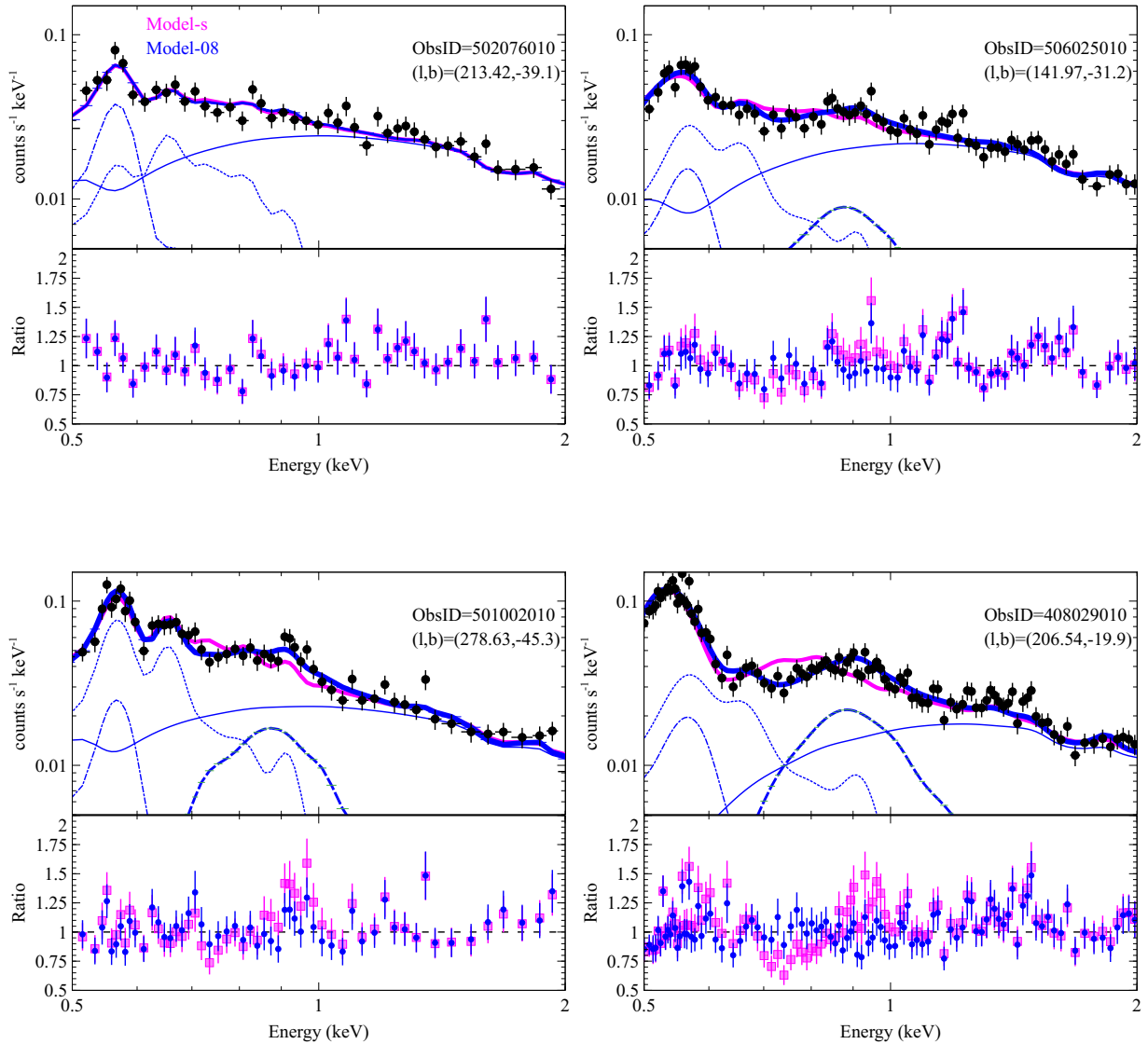


Fig. 1. (upper panels) Representative XIS1 spectra (ObsID=502076010, 506025010, 501002010, 408029010) fitted with Model-s (thick magenta lines) and Model-08 (thick blue lines). The thick blue dashed lines show the contributions of the 0.8 keV component. The thin blue solid, dotted, and dot-dashed lines correspond to the contributions of CXB, MWH, and LBH, respectively, to the best-fit Model-08. (bottom panels) The data-to-model ratio for Model-s (filled magenta squares) and Model-08 (filled blue circles).

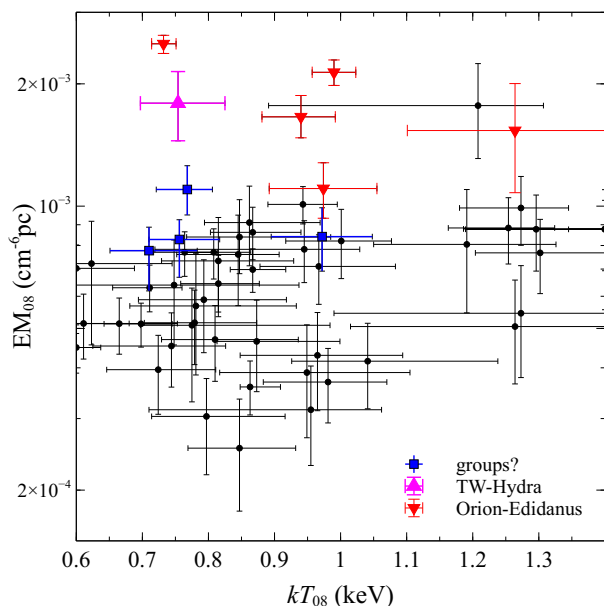


Fig. 2. Temperature of the 0.8 keV component plotted against EM_{08} with Model-08-kTfree for the observation with $\Delta C < -9$. Squares indicate possible group candidates (see section 4.2), and up and down triangles correspond to TW Hya (section 3.3) and regions toward Orion-Eridanus superbubble (sections 3.3 and 4.5), respectively.

the Ori OB1 association and spanning $20^\circ \times 45^\circ$ in the sky. The observation with ObsID=408029010 ($l=206.54$, $b=-19.93$, bottom-right panel of figure 1), which toward the superbubble, has the brightest 0.8 keV component. EM_{08} of other four regions toward the bubble, ObsID=702062010 ($l=211.76$, $b=-32.06$), ObsID=706013010 ($l=174.83$, $b=-44.51$), ObsID=407045010 ($l=201.05$, $b=-31.29$), and ObsID=409029010 ($l=192.85$, $b=-48.96$) also have $EM_{08} > 10^{-3} \text{ cm}^{-6} \text{ pc}$ (figure 2). EM_{08} around a T Tauri star, TW Hya ($l=278.66$, $b=22.96$, ObsID=402089020), is the third brightest among the 130 observations. In some cases, nearby regions show significantly different EM_{08} . For example, the EM_{08} of a region ($l=213.42$, $b=-39.1$, ObsID=502076010) near the Orion-Eridanus superbubble is consistent with zero (the top left panel of figure 1).

Figure 4 shows EM_{08} for Model-08 plotted against the absolute value of Galactic longitude, $|l|$, and latitude, $|b|$. Here, $|l|$ is defined as l for $0^\circ \leq l < 180^\circ$ and $(360^\circ - l)$ for $180^\circ \leq l < 360^\circ$. For a given longitude or latitude, there is a significant scatter of an order of magnitude in EM_{08} . As shown in table 1, the median value of the low latitude sample ($|b| < 35^\circ$) is a factor of 1.3 and 2 higher than those of the mid-latitude ($35^\circ < |b| < 50^\circ$) and high-latitude samples ($|b| > 50^\circ$), respectively, although the 16th-84th percentile ranges overlap significantly. There is no significant dependence of EM_{08} on $|l|$.

3.4 Correlation with the solar activity

Our data were obtained from 2005 to 2015, covering almost one solar cycle, including the solar minimum around 2009 and the solar maximum around 2014. Therefore, they are suitable for studying the contributions of SWCX. Fujimoto et al. (2007) found strong O/Ne/Mg line emission from geocoronal SWCX with Suzaku. In addition to the time-variable O VII, O VIII, Ne X, and Mg XI emission lines, they also detected features in the 0.75-0.95 keV energy range. Although we screened the data using lightcurves, these SWCX emissions may remain and contribute to the 0.8 keV component. In addition, it is not easy to filter the heliospheric SWCX emissions, whose time variations are expected to be slow. In figure 4, we plot EM_{08} for Model-08 against the Galactic latitude with the 13-month-smoothed sunspot number (hereafter SSN) from the World Data Center SILSO, Royal Observatory of Belgium, Brussels (SILSO 2005–2015)¹ in the color scale. Figure 5 shows EM_{08} plotted against the observation date with SSN. The scatter in EM_{08} is large, and the correlation with the solar activity is relatively small. The median value of EM_{08} for the data obtained before the end of 2009 (hereafter 2005–2009 data), $\sim 3 \times 10^{-4} \text{ cm}^{-6} \text{ pc}$, is slightly lower than $\sim 4 \times 10^{-4} \text{ cm}^{-6} \text{ pc}$ for the remaining data (hereafter 2010–2015 data), as shown in table 2, although the 16th–84th percentile ranges overlap significantly.

The heliospheric SWCX is expected to be stronger near the ecliptic plane (Robertson & Cravens 2003; Koutroumpa et al. 2006). Figure 6 shows EM_{08} values of the 130 observations plotted against the absolute value of the ecliptic latitude, with the color scale of the 13 months averaged sunspot number. There is no clear dependence of EM_{08} on the ecliptic latitude.

3.5 Spectral fitting with the SWCX emission lines

Paper-I reported that fitting the 2005–2009 data with Model-08 resulted in fairly uniform values of kT_{halo} with the median value of 0.22 keV. In contrast, for the 2010–2015 data, Model-08 gives lower values of kT_{halo} . They concluded that during the solar maximum period, excess emissions of the O VII He α line possibly from the heliospheric SWCX cause an underestimation of kT_{halo} and an overestimation of EM_{halo} . Therefore, we added a Gaussian with the fixed central energy of 0.56 keV for the O VII He α line to Model-08, fixing kT_{halo} at 0.22 keV, and re-fitted the spectra of the 130 observations. We will refer to this model as Model-08+OVII. The differences in EM_{08} between the

¹ SILSO, World Data Center—Sunspot Number and Long-term Solar Observations, Royal Observatory of Belgium, on-line Sunspot Number catalogue (2005–2015) <<http://www.sidc.be/SILSO/>>

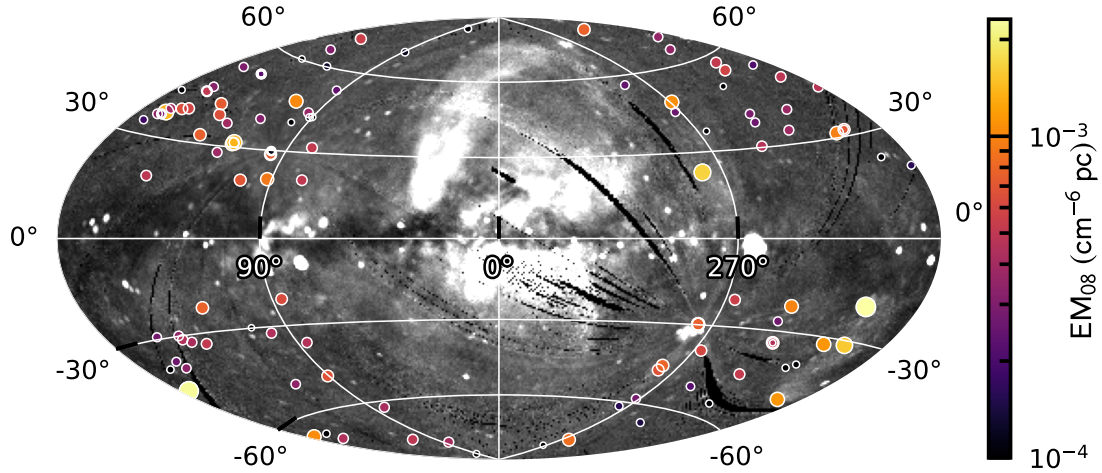


Fig. 3. The 3/4 keV band image of the ROSAT all-sky survey. The color and size of the marks indicate EM_{08} with Model-08.

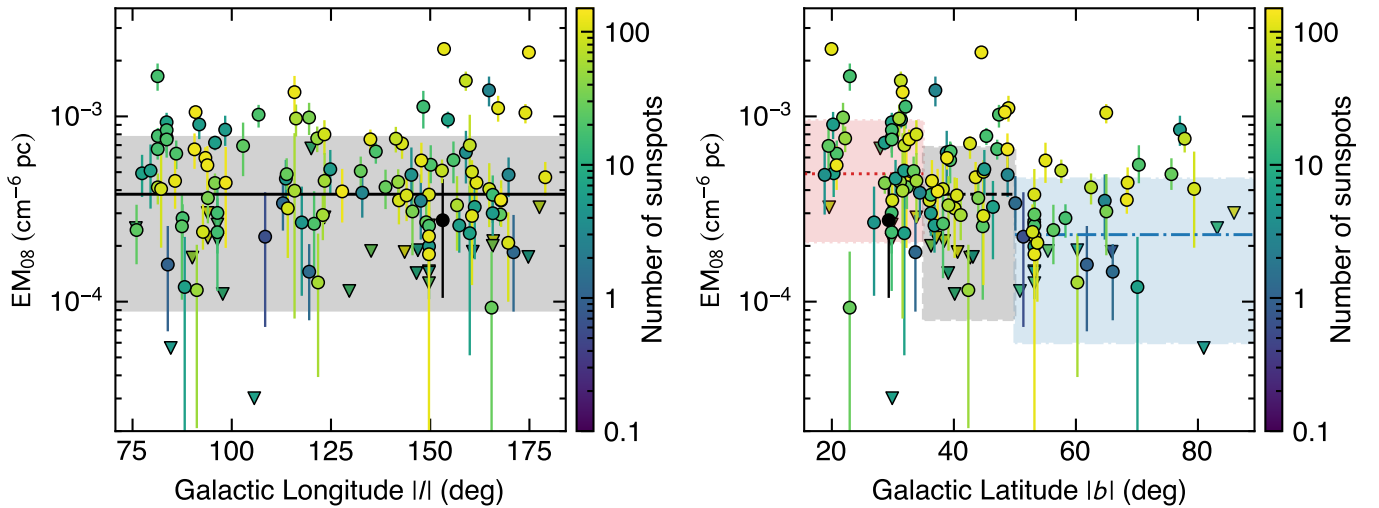


Fig. 4. (left) EM_{08} with Model-08 plotted against the absolute value of the Galactic longitude, $|l|$. The color scale corresponds to the 13-month smoothed sunspot number. The shaded region shows the median and the 16th-84th percentile range for the 130 observations. The triangles show the 1σ upper range. (right) Same as the left panel but plotted against the absolute value of the Galactic latitude, $|b|$. The shaded regions show the medians and 16th-84th percentile ranges for the observations at $|b| \leq 35^\circ$, $35^\circ < |b| \leq 50^\circ$, and $|b| > 50^\circ$.

two model fits are up to $\sim 1.5 \times 10^{-4} \text{ cm}^{-6} \text{ pc}$, which is much smaller than the scatter in EM_{08} for Model-08. As shown in the left panel of figure 7, when kT_{halo} for Model-08 is higher than 0.23 keV, EM_{08} for Model-08+OVII increases from that for Model-08. With Model-08, an overestimation of kT_{halo} lead to an underestimation of EM_{08} . In contrast, for the data with $kT_{\text{halo}} < 0.19$ keV, EM_{08} for Model-08+OVII decreases from that for Model-08.

Our sample includes nine data toward Lockman Hole (LH) data obtained from 2006 to 2014, covering almost one solar cycle, with nearly the same lines of sight. Suzaku also observed the North Ecliptic Pole (NEP) in 2005, 2006, and four times in 2009 (whose pointings are $1^\circ.2$ offset from those obtained in 2005 and 2006) and the South Ecliptic

Pole (SEP) four times in 2009. As shown in figure 7, EM_{08} with nearly the same pointing are more consistent with each other for Model-08+OVII than for Model-08. In particular, the scatter in EM_{08} is reduced for the LH data, while the weighted averages of EM_{08} from the two models are almost the same at $(1.6 \pm 0.3) \times 10^{-4} \text{ cm}^{-6} \text{ pc}$. The left and middle panels of figure 8 show the plots EM_{08} against EM_{halo} with Model-08 and Model-08+OVII, respectively. The 16th-84th percentile ranges of EM_{08} for the 2005-2009 and 2010-2015 data become more consistent with Model-08+OVII than those for Model-08 (table 2). These consistencies in EM_{08} with Model-08+OVII indicate that the 0.7-1 keV residual structures detected in some regions are unlikely to be caused by the remaining SWCX emissions

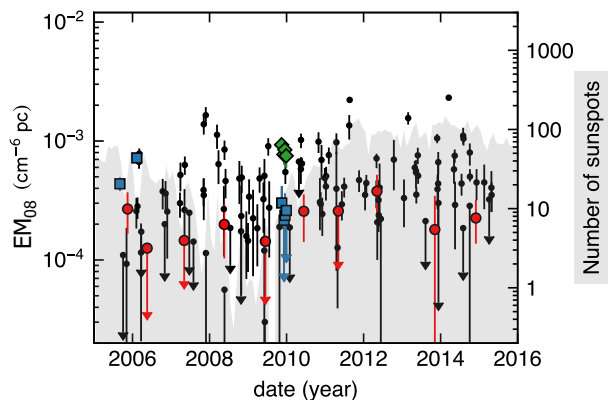


Fig. 5. EM_{08} plotted against the observation date. The 13-month averaged sunspot number, SSN, is also shown as the gray-shaded area. The filled circles, squares, and diamonds are LH, NEP, and SEP, respectively. The data with the lower triangles show an upper range of 1σ .

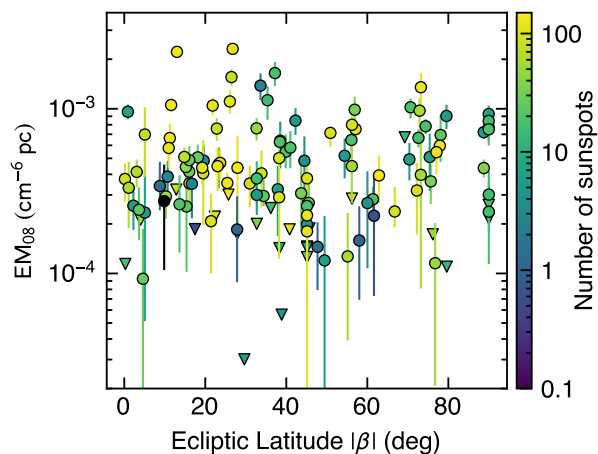


Fig. 6. EM_{08} plotted against the absolute value of the ecliptic latitude, β . The color scale indicates the 13-month averaged sunspot number.

in this energy band. As reported by Paper-I, EM_{halo} with Model-08 depends on the solar activity (table 2 and the left panel of figure 8). As plotted in the middle panel of figure 8, with Model-08+OVII, the scatter in EM_{halo} is significantly reduced, and the 16th-84th percentile ranges for the two epochs become consistent.

With XMM-Newton observations, Qu et al. (2022) reported that the O VIII Ly α line emissions from the heliospheric SWCX also contaminate the spectra. Therefore, we added another Gaussian at 0.65 keV for O VIII Ly α to Model-08+OVII and re-fitted the spectra. Here we assumed that the normalization of the Gaussian at 0.65 keV is 20% of that at 0.56 keV. This ratio is derived from the excess emission from the Lockman Hole data obtained in 2013 at the solar maximum compared to that obtained in 2009 at the solar minimum (Paper-I). We will

refer to this model as Model-08+OVII/OVIII. The differences in EM_{08} are up to $\sim 1.5 \times 10^{-4} \text{ cm}^{-6} \text{ pc}$. However, for the data with $kT_{\text{halo}} < 0.19 \text{ keV}$ for Model-08, Model-08+OVII/OVIII gives almost the same EM_{08} with Model-08. With this model, the median and the 16th-84th percentile range of EM_{08} are similar to those for Model-08 (table 2 and figure 8). Although the error bars of the individual observations are relatively large, EM_{08} with nearly the same lines of sight are more consistent for Model-08+OVII than those for Model-08+OVII/OVIII. As shown in figure 7, when kT_{halo} for Model-08 is higher than 0.23 keV, EM_{08} for Model-08+OVII/OVIII also increases from that for Model-08. For each observation, it is difficult to determine whether Model-08+OVII or Model-08+OVII/OVIII is more appropriate. The differences in EM_{08} from the three models are up to $1.5 \times 10^{-4} \text{ cm}^{-6} \text{ pc}$. We will treat this value as a systematic error in EM_{08} .

4 Discussion

We analyzed the Suzaku data of the 130 observations toward $75^\circ < l < 285^\circ$ and $|b| > 15^\circ$. Our sample does not include the eROSITA bubble (Predehl et al. 2020), bright regions toward the north and south of the Galactic center. With the standard soft X-ray background model consisting of LHB and MWH, residual structures remain in the spectra of some regions at 0.7–1 keV. For 56 out of the 130 observations, adding a spectral component with $kT \sim 0.8 \text{ keV}$, which is much higher than the virial temperature of the Milky Way, gives better fits than the standard soft X-ray background model. This component tends to be brighter toward the lower Galactic latitude. A similar superviral temperature component has been detected with the HaloSat observations of 85% of the field at $|b| > 30^\circ$ (Bluem et al. 2022). The EM_{08} around the eROSITA bubble observed with Suzaku tends to be higher than the other regions (Gupta et al. 2023). Excluding the eROSITA bubble, the detection rate of EM_{08} with HaloSat becomes closer to ours. Beyond 100° from the Galactic center, the median value of EM_{08} with HaloSat is $\sim 10^{-3} \text{ cm}^{-6} \text{ pc}$. This value corresponds to $\sim 4 \times 10^{-4} \text{ cm}^{-6} \text{ pc}$ for the solar abundance table we use and is consistent with our median value.

Paper-I reported that kT_{halo} and EM_{halo} become fairly uniform toward the Galactic anti-center sky and at high Galactic latitude and suggested that the virial temperature plasma fills the Milky Way halo. As shown in figure 8, the scatter in EM_{08} is significantly larger than that in EM_{halo} . Therefore, it is reasonable to assume that the MWH component is smoothly distributed in the halo and that the 0.8 keV component has a different origin than the

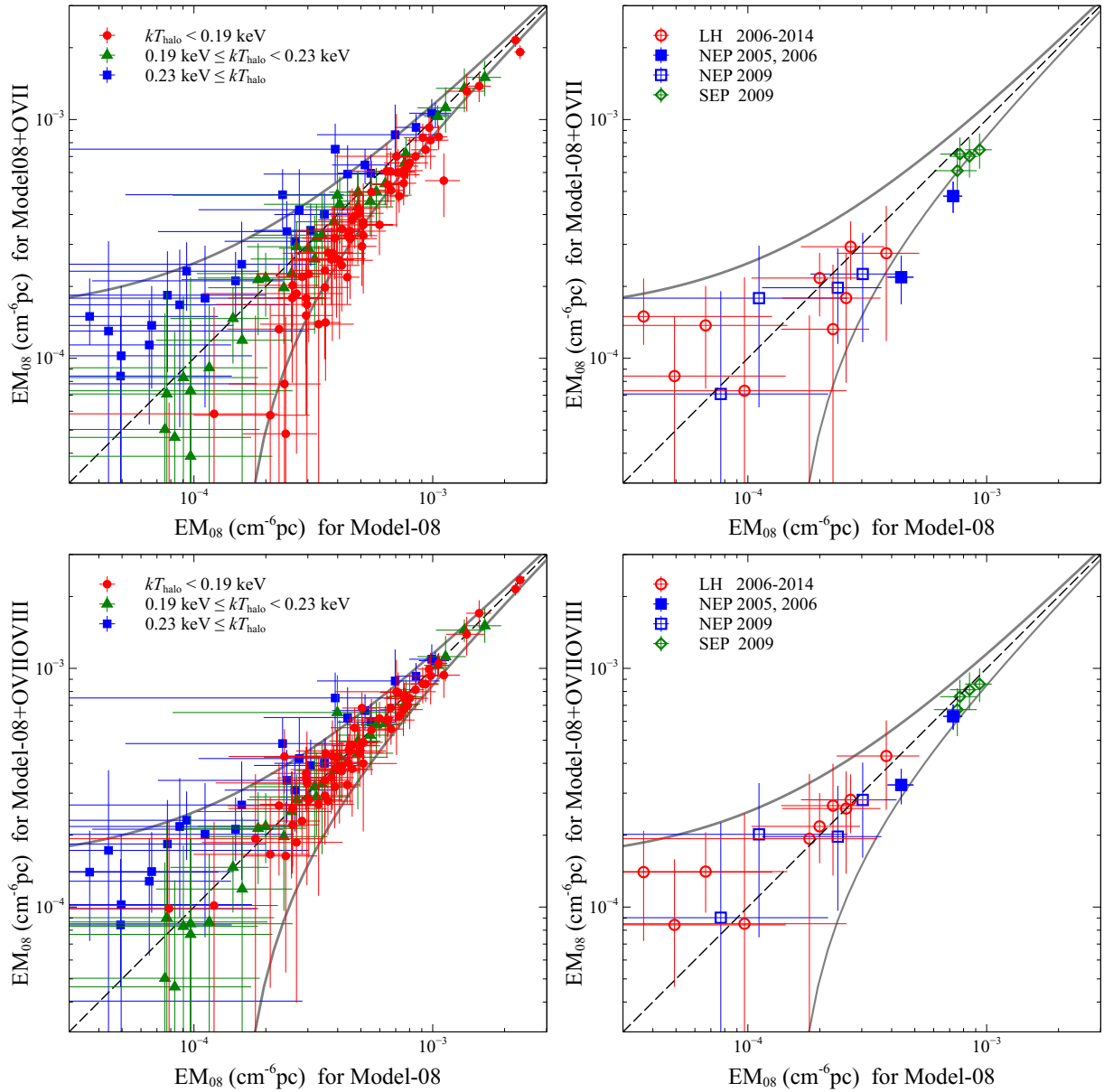


Fig. 7. (top left panel) EM_{08} with Model-08+OVII plotted against those with Model-08 for the data with $kT_{\text{halo}} < 0.19$ keV (filled circles), $0.19 \text{ keV} \leq kT_{\text{halo}} < 0.23$ keV (filled triangles), and $kT_{\text{halo}} > 0.23$ keV (filled squares). The dashed line is the line of equality, and the gray solid lines show the difference of $1.5 \times 10^{-4} \text{ cm}^{-6} \text{ pc}$. (top right panel) The same as the left panel but for LH (open circles), NEP (2005-2006; filled squares), NEP (2009; open squares), and SEP (open diamonds). (bottom panels) Same as the top panels but for Model-08+OVII/OVIII.

Table 2. Medians and 16th-84th percentile ranges of EM_{halo} and EM_{08}

model	selection	N*	EM_{halo}		EM_{08}	
			median $10^{-3} \text{ cm}^{-6} \text{ pc}$	16th-84th percentile $10^{-3} \text{ cm}^{-6} \text{ pc}$	median $10^{-4} \text{ cm}^{-6} \text{ pc}$	16th-84th percentile $10^{-4} \text{ cm}^{-6} \text{ pc}$
Model-08	2005-2009	64	2.4	1.4–5.5	2.8	0.7–7.5
Model-08	2010-2015	66	6.8	2.9–13.0	4.2	2.0–7.8
Model-08+OVII	2005-2009	64	2.0	1.4–3.7	2.9	0.9–6.3
Model-08+OVII	2010-2015	66	3.0	1.8–4.4	3.4	1.1–7.2
Model-08+OVII/OVIII	2005-2009	64	1.9	1.3–3.3	2.9	1.0–6.7
Model-08+OVII/OVIII	2010-2015	66	2.4	1.0–3.7	4.5	2.0–8.4

* Number of observations

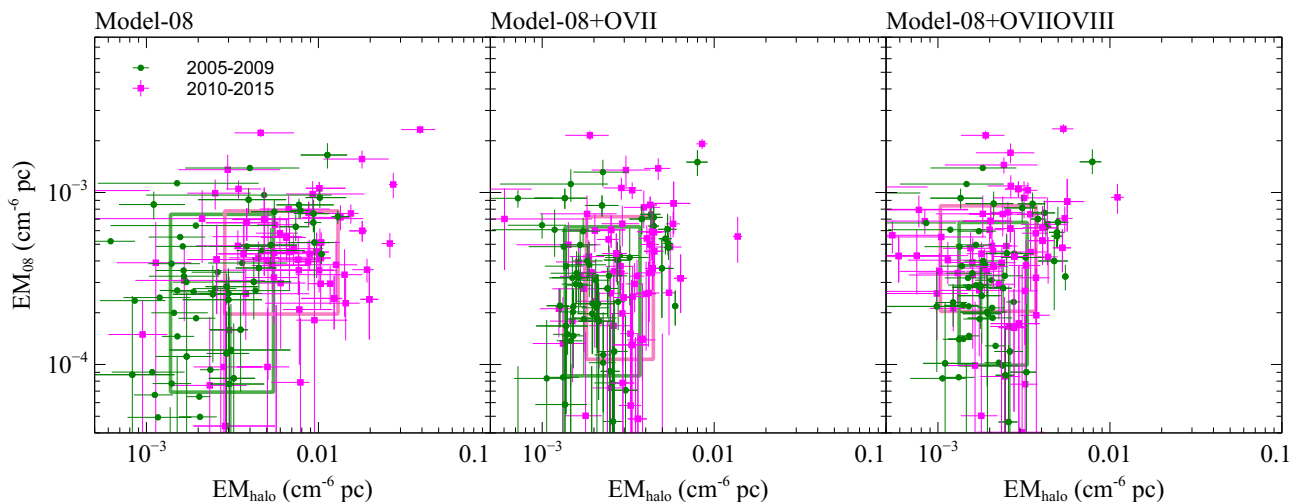


Fig. 8. EM_{08} with Model-08 (left panel), with Model-08+OVII (middle panel), and with Model-08+OVII/OVIII (right panel) plotted against EM_{halo} . Circles and squares correspond to the data taken before and after, respectively, the end of 2009. The light magenta and green boxes show the 18th-84th percentile ranges for the 2005-2009 and 2010-2015 data, respectively.

MWH component.

4.1 Contamination of unresolved stars

The spectra of the 0.8 keV component resemble those of stars. Masui et al. (2009) found a CIE component with a temperature of ~ 0.8 keV in the direction of $(l, b) = (235^\circ, 0^\circ)$ with Suzaku. The spectral shape and emission measure of this component are consistent with a sum of unresolved faint dM stars. Yoshino et al. (2009) also detected a similar spectral shape component from a Suzaku observation toward $b \sim 10^\circ$. However, its emission measure is a factor of 5 higher than the predicted value of the contribution from dM stars, taking into account the expected decrease in the stellar surface brightness toward the higher Galactic latitudes. The emission measure of this $b = 10^\circ$ component is similar to those of our sample at $|b| = 15^\circ \sim 20^\circ$.

The total resolved stellar flux toward the Chandra Deep Field South ($l = 224^\circ, b = -54^\circ$) down to $5 \times 10^{-18} \text{ ergs}^{-1} \text{ cm}^{-2}$ is about a few percent of that from AGNs in the 0.5–2.0 keV energy band (Lehmer et al. 2012). This stellar contribution is equivalent to $EM_{08} \sim 10^{-4} \text{ cm}^{-6} \text{ pc}$. The weighted average of EM_{08} from the nine LH observations ($l = 150^\circ, b = 53^\circ$) is $(1.6 \pm 0.3) \times 10^{-4} \text{ cm}^{-6} \text{ pc}$ for both Model-08 and Model-08+OVII. This value is marginally consistent with the stellar contribution from the Chandra observations with similar $|l|$ and $|b|$. The EM_{08} of the LH observations is one of the lowest among the 130 observations. A significant fraction of the observations at $|b| > 50^\circ$ show much higher EM_{08} .

At $|b| = 30^\circ$, the integrated star count with 2MASS is a factor of \sim two higher than that at $|b| \sim 50^\circ$ (Chang et al. 2011). Assuming that the stellar contribution to the 0.8 keV component is proportional to the integrated star counts, EM_{08} at $|b| \sim 30^\circ$ from stars is about a few times $10^{-4} \text{ cm}^{-6} \text{ pc}$, which is lower than the median value of EM_{08} at $35^\circ < |b| < 50^\circ$.

If the excitation radius for bright sources is small, their scattered photons can contaminate the spectra. For example, there are two bright stars in the FOV of the 2005 LH observation, which is offset by $0^\circ.5$ from the other LH observations. When the excitation radius is $1'$, the best-fit value of EM_{08} for the 2005 data, $6 \times 10^{-4} \text{ cm}^{-6} \text{ pc}$, is significantly higher than those for the other LH observations. In this paper, the excitation radius of $2'.5 \sim 3'$ is adopted for these stars. Then, the derived EM_{08} , $(2.7 \pm 1.0) \times 10^{-4} \text{ cm}^{-6} \text{ pc}$, is consistent with the weighted average value of EM_{08} of the other LH observations. Finally, if the contribution of the faint stars is significant, we expect a smoother distribution of EM_{08} . Thus, the stellar contribution to the 0.8 keV component is relatively small.

4.2 Contamination of background groups of galaxies

The spectrum of the 0.8 keV component also resembles those from intracluster medium (ICM) in groups of galaxies. If the hot gas has an extragalactic origin, we expect a uniform distribution of the hot gas blob without dependence on the Galactic latitude and longitude. Therefore, the background groups and clusters of galaxies may not be

the primary origin of the 0.8 keV component. However, regions with the brightest EM₀₈, especially at high latitudes, may be related to the ICM emission from galaxy groups. The 0.8 keV galaxy groups typically have r_{500} of ~ 0.4 Mpc (Sun et al. 2009; O’Sullivan et al. 2017). Here, r_{500} is the radius of a sphere whose mean enclosed density is 500 times the critical density of the Universe. At $z = 0.03$, this radius is ~ 11 arcmin. Since the 0.8 keV component extends across the FOV of the XIS detectors, we searched for concentrations of galaxies at $z < 0.03$ in each FOV with $\Delta C < -9$. There are two Hickson compact groups (Hickson 1982), HCG 16 at $z=0.012$, HCG 96 at $z=0.029$, and two groups at $z=0.029$ and 0.015 (Díaz-Giménez & Zandivarez 2015; Garcia 1993) in the FOVs of observations with ObsID=709009010, 708023010, 703016010, 708002010, respectively.

4.3 Modeling of the spatial distribution of the 0.8 keV component

Figure 9 shows EM₀₈ plotted against $|b|$, separated into four $|l|$ ranges. The scatter in EM₀₈ toward the Galactic anticenter ($165^\circ < |l| < 180^\circ$) is relatively small, except for one possible group candidate (ObsID=709009010, $l = 174^\circ$, $b = -65^\circ$, section 4.2) and the two regions toward the Orion-Eridanus superbubble within this $|l|$ range. We model the spatial distribution of the 0.8 keV component, assuming that it is a CIE plasma. The possible dependence of EM₀₈ on $|b|$ suggests that the emissivity increases toward the disk. Therefore, we compare the obtained EM₀₈ distribution with the following disk-like gas model,

$$n_e = n_{e0} \exp\left(-\frac{R}{R_0}\right) \exp\left(-\frac{z}{z_0}\right) \quad (1)$$

Here, n_e is the electron number density, n_{e0} is that at the Galactic center, R is the distance from the Galactic center projected onto the Galactic plane, z is the vertical height, R_0 and z_0 are the scale length and scale height, respectively. Assuming the distance from the Solar System to the Galactic Center to be 8 kpc, we fit the EM₀₈ distribution of the 130 observations by integrating the equation 1. Since it is difficult to constrain R_0 and z_0 , we fixed R_0 at 3 kpc and z_0 at 0.3 kpc, which are close to those of the thin disk (Chang et al. 2011; Cautun et al. 2020), and estimated $n_{e0}f_{08}^{1/2}$. Here, f_{08} is the volume filling factor of the 0.8 keV component. The fit is unacceptable with $\chi^2/\text{d.o.f.}=1372/129$, as shown in table 3 and figure 9. We then excluded the five regions toward Orion-Eridanus superbubble, TW Hydrae, and the four group candidates (see section 4.2 in detail). The fit is still not acceptable with $\chi^2/\text{d.o.f.}=744/119$. To account for possible systematic uncertainties caused by contamination of the SWCX (sec-

tion 3.5), we added systematic errors of $1.5 \times 10^{-4} \text{ cm}^{-6} \text{ pc}$ to each EM₀₈. This reduced χ^2 significantly reduced to $\chi^2/\text{d.o.f.}=197/119$. As summarized in table 3, $n_{e0}f_{08}^{1/2}$ does not depend on the sample selection and systematic uncertainties. Assuming $R_0 = 7$ kpc, which is the value adopted for the MWH component in Paper-I, $n_{e0}f_{08}^{1/2}$ decreases by about a factor of 5. However, around the solar system, or at $R=8$ kpc and $z=0$ kpc, the two R_0 cases yield almost the identical values of $n_e f_{08}^{1/2} = (1.3 - 1.4) \times 10^{-3} \text{ cm}^{-3}$. If we allow z_0 to vary, fixing R_0 at 7 kpc, we get $z_0 = 1.9 \pm 1.2$ kpc. Although $n_{e0}f_{08}^{1/2}$ depends strongly on R_0 and z_0 , at $R = 8$ kpc, and $z = 0.3$ kpc, all the five fits give almost the same value of $n_e f_{08}^{1/2} = 0.5 \times 10^{-3} \text{ cm}^{-3}$.

4.4 Physical properties of the 0.8 keV component

The median values of the emission measures of the 0.8 keV and MWH components for the 2005-2009 data are $(2.8 - 2.9) \times 10^{-4} \text{ cm}^{-6} \text{ pc}$ and $(2.0 - 2.4) \times 10^{-3} \text{ cm}^{-6} \text{ pc}$, respectively, with the three models, Model-08, Model08+OVII, and Model-08+OVII+OVIII (table 2). If the two components follow the same spatial distribution and are in pressure equilibrium, f_{halo} is a factor of $\sim 1.5 - 2$ smaller than f_{08} . Here, f_{halo} is the volume filling factor of the MWH component, and we assume the temperature of the two components at 0.8 keV and 0.22 keV. If this is true, then the 0.8 keV component fills a larger spatial volume than the MWH component, and we expect a smoother distribution for the 0.8 keV component than for the MWH component. However, the EM_{halo} is quite uniform compared with EM₀₈ (figure 8). Paper-I reported that the emission distribution of the MWH component at $|l| > 105^\circ$ is well represented by a sum of disk-like and spherical morphology components. If a significant fraction of the MWH component comes from the latter, the scatter in EM_{halo} may be small.

The scatter in EM₀₈ suggests a relatively small value of f_{08} . There are other ISM components in the Milky Way. At the midplane, most of the volume is filled with neutral medium: assuming turbulent pressure equilibrium, its volume filling factor is estimated to be about 0.6, and that for the hot ionized medium is only about 0.2 (Kalberla & Kerp 2009). They also estimated the vertical structure of these media: at $z = 0.5$ kpc, the volume filling factor of the hot gas reaches 0.3–0.4. Above the midplane, the volume filling factor of the warm ionized medium (WIM), or H α -emitting gas, increases, and at $z \sim 0.5 - 1$ kpc, peaking at about 0.3. The pressure of WIM is estimated to be $p/k \sim 5000 \text{ cm}^{-3} \text{ K}$ and a few thousand $\text{cm}^{-3} \text{ K}$ at the midplane and at $z = 0.3$ kpc, respectively (Gaensler et al. 2008). Above this height, a hot ionized medium is expected

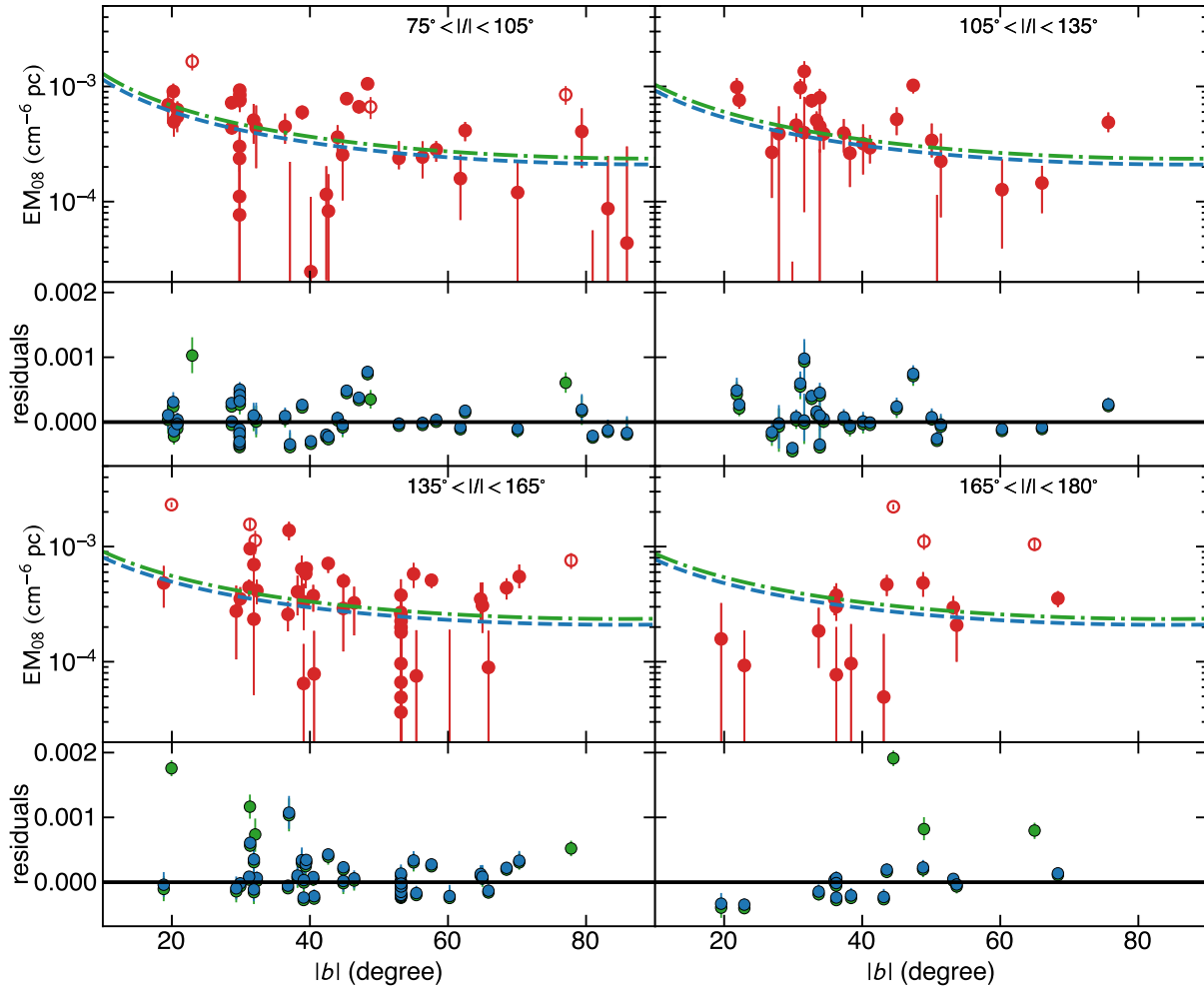


Fig. 9. EM_{08} with Model-08, plotted against the Galactic latitude, $|b|$, separated into four $|l|$ ranges. The dot-dash and the dashed lines show the best-fit disk-like morphology models ($R_0 = 3$ kpc and $z_0 = 0.3$ kpc) for all data (filled and open circles for the upper panels and open circles for the bottom panels) and those excluding the regions toward Orion-Eridanus superbubble, TW Hya, and possible candidates of groups of galaxies (plotted as open circles), respectively. The bottom panels show the residuals.

Table 3. Fitting results of the density distribution models

selection	N^*	$n_{e0} f_{08}^{1/2 \dagger}$ (10^{-3}cm^{-3})	R_0 (kpc)	z_0 (kpc)	$\chi^2/\text{d.o.f}$
all	130	19 ± 1	3.0 (fix)	0.3 (fix)	1372/129
all - bright regions [‡]	120	18 ± 1	3.0 (fix)	0.3 (fix)	744/119
all - bright regions ^{‡§}	120	20 ± 1	3.0 (fix)	0.3 (fix)	197/119
all - bright regions ^{‡§}	120	4.2 ± 0.1	7.0 (fix)	0.3 (fix)	199/119
all - bright regions ^{‡§}	120	1.8 ± 0.5	7.0 (fix)	1.9 ± 1.2	194/118

* Number of observations

† The central electron density (n_{e0}) of the disk model, assuming the metal abundance of 1 solar. f_{08} is the volume filling factor of the 0.8 keV component.

‡ The five regions toward the Orion-Eridanus superbubble, one toward TW Hya, and four toward group candidates were excluded from the sample.

§ A systematic error of $1.5 \times 10^{-4} \text{cm}^{-6} \text{pc}$ is added in quadrature to each EM_{08} .

to fill more than half of the volume.

Adopting the best-fit disk-like and spherical morphology model for the MWH component in Paper-I and the disk-like model for the 0.8 keV component, we can estimate the electron density, cooling time, and pressure. At $R = 8$ kpc and $z = 0.3$ kpc, $n_e f_{08}^{1/2} = 0.5 \times 10^{-3} \text{ cm}^{-3}$ and $n_{e,022} f_{\text{halo}}^{1/2} = 10^{-3} \text{ cm}^{-3}$. Here, $n_{e,022}$ is the electron density of the MWH component. Then, the radiative cooling time of the 0.8 keV component is $7 f_{08}^{1/2}$ Gyr. The pressures, p , of the 0.8 keV and MWH components are $p/k \sim 9000 f_{08}^{-1/2} \text{ cm}^{-3} \text{ K}$ and $5000 f_{\text{halo}}^{-1/2} \text{ cm}^{-3} \text{ K}$, respectively. If these two components are in pressure equilibrium, f_{08} is a factor of three larger than f_{halo} . Assuming that the volume filling factor of the hot gas (MWH and 0.8 keV) is 0.25, the hot gas pressure reaches $20000 \text{ cm}^{-3} \text{ K}$, which is much higher than the thermal pressure of WIM. Considering that the temperature of the 0.8 keV component is significantly higher than the virial temperature and its long cooling time and high pressure, it can escape from the Galactic disk.

4.5 The Orion-Eridanus superbubble

Among the observations with the largest EM_{08} , five are toward the Orion-Eridanus superbubble around $(l, b) \sim (200^\circ, -40^\circ)$. This superbubble is a nearby (~ 400 pc) and well-known feature of the soft X-ray background spanning $20^\circ \times 45^\circ$ on the sky (e.g. Reynolds & Ogden 1979, Burrows et al. 1993, Snowden et al. 1995), and possibly a large cavity extending from the Ori OB1 association. Burrows et al. (1993) reported that a 0.1–0.2 keV plasma fills the interior of the superbubble, which extends ~ 200 pc from the Galactic disk. The cavity is thought to be formed from SN remnants, UV radiation, or stellar wind from the Orion OB1 association. The enhancement of the 0.8 keV component toward the Orion-Eridanus superbubble indicates that a hotter plasma is also likely to exist in the bubble. With HaloSat observations, Fuller et al. (2023) detected a hot plasma with a temperature of 0.79 ± 0.12 keV. The pressure of this component is estimated to be $(3\text{--}5) \times 10^4 \text{ cm}^{-3} \text{ K}$, which is a factor of two higher than that of the 0.8 keV component at $R = 8$ kpc and $z_0 = 0.3$ kpc. Numerical simulations expect that young star clusters form superbubbles whose evolution is quite different from those of each SN (e.g. Keller et al. 2014, Sharma et al. 2014). These simulations suggest that SNe in star clusters may heat some gas to ~ 1 keV, whose cooling time is much longer than 10^8 yr. If so, the Orion OB1 association may have produced hot plasma with a temperature of ~ 1 keV.

4.6 The origin of the 0.8 keV component

Strong emissions with a temperature of about 1.3 keV are seen in the Galactic ridge spectra at $2^\circ < |l| < 30^\circ$ and $|b| < 1^\circ$ (Uchiyama et al. 2013). The estimated electron density of this ridge component is about $2 \times 10^{-3} \text{ cm}^{-3}$, which is close to n_{e0} of the 0.8 keV component if it has a relatively large R_0 , about 7 kpc. In spiral galaxies, the temperature component around 0.8 keV is sometimes detected in addition to the 0.2–0.3 keV component (e.g. Mineo et al. 2012, Weżgowiec et al. 2020). The estimated n_e of the 0.8 keV component in our analysis is comparable to that for other spiral galaxies such as M83 (Weżgowiec et al. 2020). These results suggest that the 0.8 keV component is common in spiral galaxies.

The enhancement of the 0.8 keV component around the Orion-Eridanus superbubble suggests that SNe or stellar wind can heat the gas to ~ 1 keV. Stars are formed in clusters, and SNe create superbubbles that are more effective at heating the interstellar medium than each SN. The temperature of the hot gas in such superbubbles reaches 1 keV, with a relatively long cooling time (Keller et al. 2014; Keller et al. 2016). This temperature is higher than the virial temperature of the Milky Way. Therefore, bubbles can leave the stellar disk and cause galactic fountains.

Based on the detection of 0.5–1 keV component, the influence of the stellar feedback has been discussed in previous studies (e.g. Nakashima et al. 2018, Bluem et al. 2022, Ponti et al. 2023). Then, we expect that EM_{08} increase toward the Galactic disk, where star formations occur. Our dataset, which focuses on $|b| > 15^\circ$, indicates a dependence on $|b|$. Although the error is large, the best-fit scale height for the 0.8 keV component, $z_0 = 1.9 \pm 1.2$ kpc, is higher than the scale height of the stellar disk. These results may be related to the recent feedback from the Galactic disk or the Galactic fountains. The scatter in EM_{08} is consistent with stellar feedback.

Paper-I reported that with Model-08, in the stacked spectra of the 130 observations, there is a residual at the line energies of the Ne Ly α line and the Mg He α line. If SNe produce a hot gas in a star-forming region, we expect an enhancement of the abundances of the α -elements (Nomoto et al. 2013). When we allow kT_{08} to vary, with Model-08-kTfree, some regions have higher temperatures around 1.3 keV. Such high-temperature regions may contribute to these Ne and Mg lines. If the hot gas is multiphase, as expected from numerical simulations (e.g., Keller et al. 2014), it is a challenge to degenerate the temperature structure and abundance pattern with the energy resolution of the CCD detectors. With *XRISM*, the successor to the *Hitomi* mission, observations of spiral galaxies will

provide a valuable opportunity to access the temperature structure and reliable abundance pattern (XRISM Science Team 2020).

5 Summary and Conclusion

We analyzed XIS data from 130 Suzaku observations at $75^\circ < l < 285^\circ$ and $|b| > 15^\circ$. We fitted the spectra with a standard soft X-ray background model consisting of the LHB and MWH. Then, there are residual structures at 0.7–1 keV in some regions. Including an additional hot CIE component with a temperature of ~ 0.8 keV gives $\Delta C < -9$ for 56 observations out of 130. EM₀₈ show a significant scatter, with the median value of $4 \times 10^{-4} \text{ cm}^{-6} \text{ pc}$ and the 16th–84th percentile range of $(1-8) \times 10^{-4} \text{ cm}^{-6} \text{ pc}$. The data were obtained from 2005 to 2015, covering nearly one solar cycle, and are suitable for studying the contamination by emissions from SWCX. Paper-I reported that the contamination of the O VII He α line, possibly from the heliospheric SWCX, sometimes leads to an underestimation of the temperature of the MWH component. From the spectral fits with the O VII He α and O VII Ly α lines with a fixed MWH temperature of 0.22 keV, we conclude that the contamination of the SWCX causes some systematic differences up to $1.5 \times 10^{-4} \text{ cm}^{-6} \text{ pc}$ in EM₀₈. Regions toward the Orion-Eridanus superbubble have the highest emission measures of the 0.8 keV component. While the scatter is large, the emission measures tend to be higher toward the lower Galactic latitude, indicating the Galactic origin of the 0.8 keV component. The median value of EM₀₈ is significantly higher than the expected stellar contribution. The 0.8 keV component is likely produced by supernovae in the Milky Way disk, possibly related to galactic fountains.

Acknowledgments

We acknowledge all members who contributed to the Suzaku project. We acknowledge support from JSPS/MEXT KAKENHI grant numbers, 16K05300 (KM), 17K05393 (KS), 18H01260 (NY).

References

Arnaud, K. A. 1996, *Astronomical Data Analysis Software and Systems V*, 101, 17

Bluem, J., Kaaret, P., Kuntz, K. D., et al. 2022, *ApJ*, 936, 72

Brown, A. G. A., Hartmann, D., & Burton, W. B. 1995, *A&A*, 300, 903

Burrows, D. N., Singh, K. P., Nousek, J. A., et al. 1993, *ApJ*, 406, 97

Cash, W. 1979, *ApJ*, 228, 939

Cautun, M., Benítez-Llambay, A., Deason, A. J., et al. 2020,

MNRAS, 494, 4291

Chang, C.-K., Ko, C.-M., & Peng, T.-H. 2011, *ApJ*, 740, 34.

Díaz-Giménez, E. & Zandivarez, A. 2015, *A&A*, 578, A61

Dekel, A. & Silk, J. 1986, *ApJ*, 303, 39

Foster, A. R., Ji, L., Smith, R. K., et al. 2012, *ApJ*, 756, 128

Fujimoto, R., Mitsuda, K., Mccammon, D., et al. 2007, *PASJ*, 59, S133

Fuller, C. A., Kaaret, P., Bluem, J., et al. 2023, *ApJ*, 943, 61

Gaensler, B. M., Madsen, G. J., Chatterjee, S., et al. 2008, *PASA*, 25, 184

Garcia, A. M. 1993, *A&AS*, 100, 47

Gupta, A., Kingsbury, J., Mathur, S., et al. 2021, *ApJ*, 909, 164

Gupta, A., Mathur, S., Kingsbury, J., et al. 2023, *Nature Astronomy*, 7, 799

Henley, D. B. & Shelton, R. L. 2013, *ApJ*, 773, 92.

Hickson, P. 1982, *ApJ*, 255, 382

Hill, A. S., Joung, M. R., Mac Low, M.-M., et al. 2012, *ApJ*, 750, 104.

Kalberla, P. M. W., Burton, W. B., Hartmann, D., et al. 2005, *A&A*, 440, 775

Kalberla, P. M. W. & Kerp, J. 2009, *ARA&A*, 47, 27.

Kavanagh, P. J. 2020, *Ap&SS*, 365, 6

Keller, B. W., Wadsley, J., Benincasa, S. M., et al. 2014, *MNRAS*, 442, 3013

Keller, B. W., Wadsley, J., & Couchman, H. M. P. 2016, *MNRAS*, 463, 1431

Koyama, K., Tsunemi, H., Dotani, T., et al. 2007, *PASJ*, 59, S23

Koutroumpa, D., Lallement, R., Kharchenko, V., et al. 2006, *A&A*, 460, 289

Lehmer, B. D., Xue, Y. Q., Brandt, W. N., et al. 2012, *ApJ*, 752, 46

Lodders, K. 2003, *ApJ*, 591, 1220

Mineo, S., Gilfanov, M., & Sunyaev, R. 2012, *MNRAS*, 426, 1870

Masui, K., Mitsuda, K., Yamasaki, N. Y., et al. 2009, *PASJ*, 61, S115

Nakashima, S., Inoue, Y., Yamasaki, N., et al. 2018, *ApJ*, 862, 34.

Nomoto, K., Kobayashi, C., & Tominaga, N. 2013, *ARA&A*, 51, 457.

O’Sullivan, E., Ponman, T. J., Kolokythas, K., et al. 2017, *MNRAS*, 472, 1482

Ponti, G., Zheng, X., Locatelli, N., et al. 2023, *A&A*, 674, A195

Predehl, P., Sunyaev, R. A., Becker, W., et al. 2020, *Nature*, 588, 227

Qu, Z., Koutroumpa, D., Bregman, J. N., et al. 2022, *ApJ*, 930, 21

Reynolds, R. J. & Ogden, P. M. 1979, *ApJ*, 229, 942

Rees, M. J. & Ostriker, J. P. 1977, *MNRAS*, 179, 541

Robertson, I. P. & Cravens, T. E. 2003, *Journal of Geophysical Research (Space Physics)*, 108, 8031

Sekiya, N., Yamasaki, N. Y., Mitsuda, K., et al. 2014a, *Suzaku-MAXI 2014: Expanding the Frontiers of the X-ray Universe*, 66

Sekiya, N., Yamasaki, N. Y., Mitsuda, K., et al. 2014b, *PASJ*,

66, L3

Sharma, P., Roy, A., Nath, B. B., et al. 2014, MNRAS, 443, 3463

Smith, R. K., Brickhouse, N. S., Liedahl, D. A., et al. 2001, ApJL, 556, L91

Snowden, S. L., Burrows, D. N., Sanders, W. T., et al. 1995, ApJ, 439, 399

Sun, M., Voit, G. M., Donahue, M., et al. 2009, ApJ, 693, 1142

Tumlinson, J., Peeples, M. S., & Werk, J. K. 2017, ARA&A, 55, 389

Ueda, M., Sugiyama, H., Kobayashi, S. B., et al. 2022, PASJ, 74, 1396, Paper-I

Uchiyama, H., Nobukawa, M., Tsuru, T. G., et al. 2013, PASJ, 65, 19

Yoshino, T., Mitsuda, K., Yamasaki, N. Y., et al. 2009, PASJ, 61, 805

Weźgowiec, M., Ehle, M., Soida, M., et al. 2020, A&A, 640, A109

XRISM Science Team 2020, arXiv:2003.04962